Pre–protostellar core properties from far–infrared observations[1]

W. D. Langer and K. Willacy

Jet Propulsion Laboratory, California Institute of Technology, MS 169-506, Pasadena, CA 91109

langer@nimba.jpl.nasa.gov

willacy@orac.jpl.nasa.gov

ABSTRACT

We present the results of far–infrared ISOPHOT observations of the pre–protostellar cores L1498, B133 and B68. Comparison of the 100 and 200 μm data suggests the presence of two dust temperatures along the line of sight. Using a two temperature model which assumes a cold central core surrounded by a slightly warmer envelope we have isolated the 200 μm emission from the cold core. We use 160 μm and 1300 μm observations where available, together with the isolated 200 μm data to derive a dust temperature for the core. We have determined the radial mass and density distributions in each core and have considered their stability by comparing the mass estimates from the 200 μm data with their virial masses. We find the cores can be divided three regions with different radial density dependences, each of which can be described by a power law $\rho \propto r^{-\alpha}$: a relatively flat inner region with $\alpha \sim 1.2$, a steeper region with $\alpha \sim 1.8$ and a very sharp outer edge with $\alpha \gtrsim 4$. These power law results are in agreement with other derivations of pre–protostellar core density profiles. The results presented here are also consistent with several different models of core evolution. In addition, we find that the inner regions of the core are less bound that the outer ones, suggesting that the outer layers are confining the central regions.

Subject headings: dust, extinction — infrared: ISM: continuum — ISM:clouds — ISM:individual:L1498, B133, B68

---

[1]Based on observations with the *Infrared Space Observatory*, an ESA project with instruments funded by ESA member states (especially the PI countries: France, Germany, the Netherlands and the UK) and with participation of ISAS and NASA.

1. Introduction

The history of star formation begins with the formation and evolution of small dark cores in molecular clouds. Traditionally these regions have been observed by high density molecular tracers such as CO, CS and NH_3 (e.g. Myers, Linke & Benson 1983; Benson & Myers 1989; Lemme et al. 1996; Benson, Caselli & Myers 1989). However chemical models show that in dense regions molecules are removed from the gas by collision with cold dust grains resulting in the formation of icy mantles which cover the grains. Observations of dark cores have demonstrated the existence of ices e.g. Ehrenfreund & Schutte (2000) and references therein, and have provided evidence for gaseous molecular depletion. For example, Mauersberger et al. (1992) and Megzer et al. (1992) found evidence for molecular depletion in NGC2024 where the peaks in molecular emission (CO and CS) were seen to be displaced from the dust continuum peaks. In contrast, NH_3 peaks were coincident with the dust emission. Similar results were obtained in NGC1333 by Lefloch et al. (1998) where the CS emission peaks were displaced from the dust continuum emission. Willacy, Langer & Velusamy (1998, hereafter Paper I) examined the molecular line and continuum emission from the dark core L1498 and found that the $C^{18}O$ is severely depleted in the center of the core where the dust emission peaks. Again the NH_3 and the dust emission peaks were coincident. The difference in behavior of these two molecules can be understood by chemical models of collapsing regions which predict that CO will be removed from the gas faster than will NH_3 (Rawlings et al. 1992). The degree of depletion in a core will increase with increasing density since the freezeout rate is proportional to the density. Consequently the core evolutionary phase immediately before and during core collapse may not be readily observable in the main molecular tracers due to their partial, or even complete, removal from the gas. Hence continuum data, tracing the dust which is unaffected by depletion is an important means of identifying and characterizing dense cold pre–collapse and collapsing regions.

The structure of a pre–protostellar core will determine its subsequent evolution, affecting the dynamics of its collapse, the timescale over which collapse occurs and the mass of the newly formed star. A knowledge of the details of core structure and formation is therefore crucial in order to make progress in our understanding of star formation. This progress requires the interplay of observational and theoretical work. Continuum studies can provide density profiles (and dust temperature profiles) of the cores which can be used to distinguish among the available theoretical models.

To trace the evolution of a pre–protostellar core through its dust emission we need observations at many wavelengths because the intensity of the dust emission is a function of several factors including the number density of the dust, its temperature, the dust compo-

sition and its emissivity. The emission intensity is especially dependent on the temperature at short wavelengths, with a small change in temperature causing a large change in the observed emission. Longer wavelengths ($\gtrsim$ 1mm) are less dependent on temperature and can therefore be used to help estimate the grain temperature more accurately than can short wavelengths. (However the emission at wavelengths much longer than 2 – 3 mm is weak and difficult to detect). In addition, the continuum emission observed comes from both the core and any envelope that surrounds it. These regions may have different temperatures and/or emission characteristics. We need to separate the foreground envelope emission from the core emission and determine the radial profile of the core. Since continuum emission lacks velocity information we need to depend on comparing observations with models.

In Paper I we presented ISOPHOT data of L1498 at 100 and 200 μm and compared our results with molecular line data for this core. We found that the continuum data peaked in the same position as the NH_3 data but that the CO, CS and CCS emission peaks were offset from the 200 μm peak, resulting in considerable depletion factors for these molecules in the center of the core. In this paper we extend our analysis of the far–infrared (FIR) emission to two other cold pre–protostellar cores: B133 and B68, and re-examine the L1498 data in order to take account of improvements to the calibration which have been made in the last two years. We make use of the 100 and 200 μm ISO data and, where available, 160 μm data from ISO and ground based 1300 μm observations. We derive density profiles and dust temperatures and compare these to current theoretical models.

2. Data reduction

We have analyzed the 100 and 200 μm emission from three pre–protostellar cores chosen from the database of Jijina, Myers & Adams (1999). Table 1 gives the physical parameters of each source. For two of the sources (B133 and B68) 160 μm data is also available and this was used to help constrain the core temperature. In addition, ground–based 1300 μm data is available for L1498 (Ward–Thompson et al. 1994) and B133 (Ward–Thompson, Motte & André 1999).

The FIR observations are taken from the ISO archive and were made using the ISOPHOT C100 and C200 modes and the standard astronomical observation template P32 for raster mapping. The data were reduced using the latest version of the ISOPHOT Interactive Analysis package (PIA version 9.0; Gabriel et al. 1997).

The calibration of the ISOPHOT data is currently thought to be accurate to within $\pm$ 20 %. As in Paper I, we checked our 100 μm map of L1498 against the IRAS map of the same

region and at the same wavelength. The maximum intensity in the ISO map is 20.5 MJy/sr (up from 12 MJy/sr in Paper I) compared to the IRAS value of 17.5 MJy/sr, confirming the ± 20% estimate of the calibration accuracy. The 200 μm data shows a similar increase in intensity compared to its value in Paper I.

In order to isolate the emission which comes from the core itself we follow the approach of Paper I. Here we describe the analysis using B133 as an example. The other two cores are treated in the same way. Figure 1(a) and (b) show the 100 and 200 μm ISOPHOT emission from B133. The emission peaks for the two wavelengths are in different places indicating that either they trace different dust components or different dust temperatures. We regridded the 100 μm data and convolved it to the 200 μm resolution and plotted the intensity of the 100 μm emission against the 200 μm emission (Figure 1(c)). The resultant scatter plot can be seen to be comprised of two components, each of which can be fitted by a straight line. A similar result was found by Laureijs et al. (1996) for a cold core in the Chameleon complex and attributed by them to a change in dust temperature along the line of sight. The flattening out of the 100 μm distribution at high 200 μm intensity levels is not due to saturation of the 100 μm pixels since the emission from the core is weak. The highest intensity 200 μm emission comes from the central regions of the core and we interpret this distribution as arising from two components of dust with different temperatures, similar to our conclusion for L1498 in Paper I. In this picture the core consists of an inner cold region traced mainly by the 200 μm emission surrounded by an outer, slightly warmer envelope traced by both the 100 and 200 μm emission.

A similar relationship is found between the 100 and 160 μm emission. Figure 2(a) shows a map of the I_{160} emission in B133. Plotting I_{160} against I_{100} we again find two components as we did in the case of the 200 μm data (Figure 2(b)). A scatter plot of the 200 and 160 μm data shows only one component (Figure 2(c)) suggesting that these wavelengths trace the same dust component.

Returning to the 100 and 200 μm emission, we separated the two temperature components of the dust by making a two component linear fit to the scatter plot in Figure 1(c) using the following approach. The best combination of fits was determined automatically by a program developed by us which considers all possible values of the break point (i.e. the value of I_{200} at which the transition between the two temperatures occurs) and calculates the total value of the chi squared for the fits. The best combination has the lowest total chi square value. The best fits to the data are shown in Figure 1(c).

In our two temperature model of the core, the total 200 μm emission is made up from a central core component, ΔI_{200} and an envelope component, I^E_{200}. The division between the two occurs at the point where the two linear fits to Figure 1(c) cross. The linear fits show

that in the envelope I_{200}^E can be determined from I_{100}. If we assume that the 100 μm emission arises solely from the envelope then we have a way of determining the I_{200}^E contribution. For B133, I_{100} is related to I_{200}^E by

$$I_{100} = 27.8 + 0.13 I_{200}^E \quad \text{MJy/sr} \tag{1}$$

Hence, the emission coming just from the central core is given by

$$\begin{aligned} \Delta I_{200} &= I_{200} - I_{200}^E \\ &= I_{200} - 7.48 I_{100} + 207.91 \quad \text{MJy/sr} \end{aligned} \tag{2}$$

ΔI_{200} is shown in Figure 1(d).

The analysis was repeated for L1498 (Figure 3) and B68 (Figure 4)

2.1. Determination of column densities

Dust emission is generally optically thin at IR and submillimeter wavelengths. The optical depth can therefore be determined from

$$\tau(\nu) = F(\nu)[\pi\theta_{\frac{1}{2}}^2 B(\nu, T_d)]^{-1} \quad (\tau << 1) \tag{3}$$

where $F(\nu)$ is the flux density within a beam of angular radius $\theta_{\frac{1}{2}}$ and T_d is the dust temperature (Hildebrand 1983). The optical depth is related to the hydrogen column density by the dust absorption cross section per hydrogen atom, σ

$$\sigma = \frac{\tau}{N_H} \tag{4}$$

where N_H is the total hydrogen column density = $N(\mathrm{H}) + 2\ N(\mathrm{H_2})$. The value of σ is uncertain and several estimates can be found in the literature. It is expected to vary with the density and composition of the dust. Cox & Mezger (1991, hereafter CM89) describe a model which takes into account some of these variables. They find a value of

$$\sigma = 7 \times 10^{-21} (Z/Z_\odot) b/\lambda^2 \quad \lambda \geq 100\ \mu\mathrm{m} \tag{5}$$

where $Z/Z_\odot$ is the heavy element abundance relative to the solar value, λ is the wavelength in microns and b is a parameter that allows for the variation of the dust opacity in different phases of the ISM. In the diffuse ISM $b = 1$ and if $Z/Z_\odot = 1$ then the CM89 model reproduces the results of Draine & Lee (1984). Moderate density gas is represented by $b = 1.9$ and corresponds to the results of Hildebrand (1983). For very cold, dense gas where ice mantles

are accumulating, and a substantial fraction of molecules may be incorporated into such mantles, CM89 suggest that a value of $b = 3.4$ is more appropriate. CM89 estimate the uncertainty in the value of σ to be of the order of a factor of 2. It would seem that since our sources are very cold ($T < 10$ K) and depletion is likely to be occurring (as previously demonstrated for L1498) that the most appropriate value of σ would be given for $b = 3.4$.

At FIR wavelengths the calculated column densities are extremely dependent on the assumed temperature. Even small changes in the temperature can result in large variations in the column density and consequently in the calculated mass. To derive the dust temperature we need another continuum tracer of the core in addition to ΔI_{200} (remember that in our model little or no 100 μm comes from the core). Using two or more I_λ we can solve to find T_d and hence the dust column density. For B133 we have, in addition to the 100 and 200 μm data, ISOPHOT data at 160 μm and ground based 1300 μm data (Ward–Thompson et al. 1999). Since the 160 μm data shows the same relation to the 100 μm data as does the 200 μm emission we can analyze it in the same way to isolate the emission from the core, ΔI_{160}. The column densities calculated from ΔI_{200}, ΔI_{160} and the 1300 μm emission are shown in Figure 5. The 200 and 160 μm data coincide for a dust temperature of $\sim$ 9K, and both agree with the 1300 μm estimate of N_H at a slightly lower dust temperature of 7 – 8 K. We have elected to use the dust temperature derived from the 160 μm data as all three wavelengths (100, 160 and 200 μm) are from the same telescope, with the data taken and reduced in the same manner. We will assume $T_d = 9$ K in all three sources, but will also discuss the consequences of using a lower value of T_d.

There are several estimates of the kinetic temperature in L1498. These all indicate that $T_K < 10$ K. Wolkovitch et al. (1997) observed 3 transitions of CCS and estimate $T_K = 8.5$ K. Fuller & Myers (1983) found $T_K = 7.7 \pm 1.3$ K from observations of HC_3N and NH_3. Fiebig (1990) used observations of several molecules with various molecular masses to arrive at $T_K = 9.6 \pm 1.3$ K. At the densities that are found in dark cores (10^4 – 10^5 cm^{-3}) it is unlikely that the dust temperature would be higher than the gas temperature. These T_K estimates therefore provide an upper limit to the dust temperature. Our choice of $T_d = 9$ K is consistent with some of the observations, but they also suggest that a lower T_d of 7.5 – 8 K could be appropriate in L1498. A lower temperature would be consistent with the dust temperature derived from comparison of the 1300 μm and ΔI_{200} data in this source. Our choice of temperature will not affect the power law distributions we derive for the mass and density of the cores (Section 2.2) since a reduction in the temperature will just result in an increase in the proportionality constant, but it will affect the absolute values of these parameters, with a lower T_d resulting in higher densities and masses. We explore the effects of $T_d = 8$ K on the calculated cores masses in Section 3.1.

2.2. Determination of the core mass and density distributions

Once the temperature has been estimated and the column density calculated, we can determine the mass of each core. Table 2 gives the radial mass distribution for $T_d = 8$ and 9K, assuming the cores to be spherical. Also shown in this table are the virial masses of the cores assuming $n \propto r^{-1}$ and $n \propto r^{-2}$, which are calculated using H_2 line widths derived from the molecular line data given in Table 5. The comparison between the masses derived from the continuum data and the virial masses is discussed in Section 3.1.

Figure 6 plots the radial mass profiles for the three cores. In each case the data can be well fitted using a cubic polynomial. The density at a radius r, can be found from

$$n(r) = \frac{1}{4\pi r^2 m_H} \frac{dM}{dr} \tag{6}$$

where m_H is the mass of the hydrogen atom and dM/dr is determined from the fit to $M(r)$. The calculated densities as a function of radius are given in Table 3 and plotted in Figure 7.

To compare our results with models of the initial conditions of star formation we have fitted the density profiles with power laws. No single power law works over the whole radius range. We found that the density profile can be divided up into up to three regimes covering the inner, middle and outer portions of the core. Each section can be described by a power law $n(r) \propto r^{-\alpha}$. Table 4 gives the values of α for each section in each core. For L1498 only two regimes are evident. The inner parts of the cores ($r < 1 - 2 \times 10^{17}$ cm) are described by $1.1 < \alpha < 1.3$. In the middle section ($1 \times 10^{17} < r < 5 \times 10^{17}$ cm) $1.7 < \alpha < 2$ and in the outer section ($r > 5 \times 10^{17}$ cm) $\alpha \gtrsim 4$.

The value of the density at any given radius depends critically on the assumed dust temperature. In the analysis above we have taken $T_d = 9$ K but choosing $T_d = 8$ K would increase the density by a factor of ~ 5. In L1498 we have an independent estimate of the density from observations of CCS by Wolkovitch et al. (1997). They found $n(H_2) \sim 2.5 \times 10^4$ cm^{-3} at $r \sim 1.5 \times 10^{17}$ cm. The uncertainties in density are probably of the order of factors of 2 or 3 due to the uncertainties in the antenna temperatures and in the collisional rates used in the LVG calculation. This result can therefore not be used to distinguish between dust temperatures of 8 and 9 K, both of which produce $n(H_2)$ values which are consistent with the molecular line values (from ΔI_{200} $n(H_2) = 1.2 \times 10^4$ cm^{-3} for $T_d = 9$K and $n(H_2)$ $= 6.3 \times 10^4$ cm^{-3} for $T_d = 8$ K).

3. Discussion

To understand the dynamical status of these cores we first check to see if they could be in virial equilibrium, or close to it, as might be expected for a pre–protostellar core. Then we compare our radial profiles to more detailed models of static, quasi–static and collapsing cores.

3.1. Core stability

The molecular line widths observed in cores can give us information about the relative contributions of thermal and non–thermal effects to the support of the core and about the virial mass of the core. All of the cores we study here have been observed using several molecules (L1498: NH_3, CS, CCS, C_3H_2, HC_7N, Kuiper, Langer & Velusamy (1996); B133: NH_3, C_3H_2, Benson et al. (1989); Jijina et al. (1999); B68: CO, NH_3, Avery et al. (1987); Jijina et al. (1999)). Table 5 gives the line widths of some of the molecules. The observed line width, Δv, is a combination of thermal (Δv_{th}) and non–thermal (Δv_{nt}) effects

$$\Delta v = (\Delta v_{th}^2 + \Delta v_{nt}^2)^{1/2} \tag{7}$$

If we have observations of at least two molecules we can determine the non–thermal line width, the kinetic temperature and hence the line width of H_2. Alternatively a temperature can be assumed and the thermal line width determined from

$$\Delta v_{th} = \frac{1}{0.425}\sqrt{\frac{kT}{m}} \tag{8}$$

where m is the mass of the molecule. In the absence of sufficient molecular data to enable us to determine the kinetic temperature for all of the cores we have assumed a temperature of 10 K and used this to determine the non thermal contribution and the H_2 line width in each core. These results are given in Table 5. In L1498 and B68 thermal pressure dominate, whereas in B133 thermal and non-thermal pressures have an almost equal contribution.

MacLaren, Richardson & Wolfendale (1988) show that a self–gravitating sphere with a power law density profile in virial equilibrium has a mass

$$M_{vir} = kR\Delta v^2 \quad \mathrm{M}_\odot \tag{9}$$

where Δv is the FWHM of H_2 in kms^{-1} and k is a constant which is dependent on the density profile of the core. MacLaren et al. use $k = 190$ for $\rho \propto 1/r$ and $k = 126$ for $\rho \propto 1/r^2$. The virial masses calculated using Equation 9 within various radii are given in Table 2. Also

One way to distinguish among the models is to compare their predicted radial density profiles with observations. In this section we compare our results to several models. We begin by comparing our data with those of other observational studies.

As discussed above we found that in all three cores the density profile can be fitted by a series of power laws. The profile flattens off towards the center of the cores and only approaches r^{-2} at $r > 10^{17}$ cm. Similar results were found by other studies of low mass cores (Ward–Thompson et al. 1994; André, Ward–Thompson & Motte 1996; Bacmann et al. 2000). Ward–Thompson et al. (1994) studied the submillimeter emission of 21 starless cores at 4 wavelengths between 1300 and 450 μm. They found $n \propto r^{-1.2}$ for $r < 6 \times 10^{16}$ cm assuming the cores to be spherical. Although our data does not cover such small radii and we see the change in power law at slightly larger radii, our results are in general agreement with those of Ward–Thompson et al..

Bacmann et al. (2000) observed starless dense cores in absorption at 7 μm using ISOCAM. Again they find two power law regimes, with the inner, flatter, density region extending out to 4×10^{16} – 1.2×10^{17} cm, depending on the core. This work also finds that some cores show very sharp outer edges, similar to those seen in our B133 and B68 results. Bacmann et al. suggest that such sharp edges may be indicative of the cores being separated from their parent molecular clouds, resulting in finite reservoirs of mass for subsequent star formation.

Shirley et al. (2000) observed several low mass cores at 850 and 450 μm using SCUBA on the JCMT. Their source list included both pre–protostellar cores and Class 0 and Class I objects. They found that the intensity profiles of pre–protostellar cores cannot be fitted by power laws, in contrast to Class I and Class 0 sources which show power law intensity distributions over large radii. In common with other observational studies they found that the density profiles of pre–protostellar cores show a flattening towards the centers of the cores at $r < 4000$ AU. In comparison to Shirley et al. (2000) our data only covers the region from 4000 AU outwards and therefore is not sensitive to the very flat regions they detect in the centers of the cores.

Absorption studies in the mid–IR using ISOCAM have been used to constrain the density profiles at the outer edges of cores (Abergel et al. 1996, 1998; Bacmann et al. 2000). These authors found that cores have very sharp edges with $\alpha \sim 3$ or 4. Here we find $\alpha \gtrsim 4$, also indicating a sharp edge to the cores. However our results are sensitive to changes in T_d at the edge of the core. For example, if T_d increases gradually at the edge of the core rather than having a sharp discontinuity between the core and envelope dust temperatures as assumed in our model, then the column density at the edge of the core will be overestimated in our model. Hence the fall off in the density distribution at large radii may be even more

shown are the core masses calculated from the FIR data for a dust temperature of both 8 and 9 K.

At present there is no evidence from line observations of infall or outflow in any of these cores. We would therefore expect their masses to be within a factor of 2 of M_{vir}. The core mass calculated from the dust observations for $T_d = 8$ K within a radius of 6×10^{17} cm is 15.8 $M_\odot$ for B133 and 14 $M_\odot$ for B68, increasing to 43 and 38 $M_\odot$ respectively for $T_d = 8$ K. L1498 has an outer radius of 4×10^{17} cm and within this the mass is 2.2 $M_\odot$ for $T_d = 9$ K and 5.9 $M_\odot$ for $T_d = 8$ K. Considering the cores as a whole, we find that the calculated masses for B133 and B68 are within the limits for stability for $T = 9$ K when compared to the virial masses calculated assuming $n \propto r^{-2}$, i.e. the cores appear to be in virial equilibrium on large scales. L1498 is also in equilibrium but only just. Its calculated mass is $\sim 0.5\ M_{vir}$, meaning that if a dust temperature of 9 K is correct the core mass is only just large enough to prevent it from expanding. At 8K, B133 and B68 have masses which are much greater than the virial mass and are therefore unstable to collapse. L1498 would be stable for this temperature, which might indicate that L1498 is slightly colder than the other two cores.

For $r < 10^{17}$ cm the situation is rather different. In this case we compared our calculated masses with the virial mass calculated assuming $n \propto r^{-1}$ since this is closer to our estimated power law for the density distribution at small radii. We find that B133 and B68 are in equilibrium at small radii for both 9 and 8 K, although the core mass is less than the virial mass for $r < 2 - 3 \times 10^{17}$ cm. If T = 8K therefore, the outer layers are unstable to collapse whereas the inner regions are in virial equilibrium suggesting the possibility that the outer layers are confining the inner region. In L1498 the calculated mass (at $T_d = 9$ K) within 10^{17} cm is much less than M_{vir} and these layers are therefore unbound and are held in place by the outer layers. At 8 K the mass in the central regions of this core is larger but still less than M_{vir}.

3.2. Comparison with theoretical models and observational studies

The dynamics of the collapse of a pre–protostellar core will be crucially affected by the physical conditions in the pre–collapse core. For example, Shu (1977) assumed collapse from a singular isothermal sphere which leads to 'inside–out' collapse, where the collapse begins in the center of the core and proceeds with a constant rate at which mass accretes onto the central object. If collapse begins before the singular isothermal state is reached then the mass accretion rate will initially be much higher (Foster & Chevalier 1993; Henriksen, André & Bontemps 1997).

ground and it subsequent evolution. They assumed that the cores developed as ambipolar diffusion allowed neutral particles to slip past the magnetic fields supporting the gas, allowing the density to build up gradually. They found that the core centers had an r^{-1} density profile initially but that further evolution resulted in $\rho \propto r^{-1.8}$. In this picture the three cores we discuss here are in the early stages of evolution and will eventually reach a state close to that of a singular isothermal sphere.

In summary then, our results are in qualitative agreement with several of the published theoretical models, all of which predict a density distribution which is relatively flat in the center of the core and steeper in the outer regions, often approaching $\rho \propto r^{-2}$. At present the observations do not allow us to differentiate among the models.

3.3. Depletion effects in L1498

In Paper I we found the peak total column density in L1498 to be $N_H^{core} = 5 \times 10^{22}$ cm^{-2} i.e. the peak H_2 column density $= 2.5 \times 10^{22}$ cm^{-2} ($N^{core}(H_2)$ is the H_2 column density calculated from ΔI_{200}). However, subsequent to publication we found an error in the calculations which increased the column density by a factor of 4π. The correct $N^{core}(H_2)$ from Paper I should therefore have been 2×10^{21} cm^{-2}. However this value needs to be modified in the light of the results presented here

In this paper changes to the calibration of the ISOPHOT data have increased I_{100} and I_{200}, resulting in an increase in ΔI_{200} compared to Paper I. We have also used a different value of σ ($= \tau/N_H$) than the Draine & Lee (1984) value used in Paper I. This new value results in a slightly lower N_H^{core} for a given τ. A third difference is the dust temperature assumed in the present calculations. Here we use $T_d = 9$ K instead of the Paper I value of 10 K, resulting in an increase in the column density. When all these factors have been taken into account we find a peak value of $N^{core}(H_2) = 4.4 \times 10^{21}$ cm^{-2} in the central core of L1498. For $T_d = 8$ K, the peak $N^{core}(H_2) = 1.2 \times 10^{22}$ cm^{-2}. The total line of sight column density is of course larger due to the envelope contribution.

Paper I estimated the degree of CO depletion in the center of L1498 by comparing the $C^{18}O$ 1-0 emission (Lemme et al. 1995) with ΔI_{200}. The CO is tracing gas from both the core and the envelope and a full assessment of the degree to which it is removed from the gas in the center of the core requires a knowledge of the dust column density in the envelope as well as the core. The column density is very sensitive to the assumed temperature, determination of which requires additional continuum observations at other, longer, wavelengths and to the value of σ assumed. A full discussion of the depletion in L1498 will be addressed in a forth-

pronounced.

Our results are therefore in qualitative agreement with previous observational studies in that they show a flattened region towards the core center. Our power law fits are in agreement with these other studies, except for Shirley et al. who have a different interpretation of the density distribution and do not find power law fits to their data.

In order to understand better the process of protostellar collapse many models have been developed to describe the initial conditions. Evans et al. (2001) have modeled the emission in pre–protostellar cores by considering them to be Bonner–Ebert spheres with power law density distributions. They also consider a self–consistent calculation of the temperature in the cores. This latter feature of the model results in colder central temperatures and higher central densities than isothermal models. In addition, the central region of relatively constant density is smaller than in isothermal models. In all cases unstable spheres were required to fit the data.

Falgarone & Puget (1985) and Chièze & Pineau des Forêts (1987) have also considered equilibrium models of thermally–supported, self–gravitating condensations. They found a core–envelope structure develops where the isothermal core is separated from the warmed envelope by a region with a steep density gradient where $n \propto r^{-\alpha}$ ($\alpha \sim 4$). Core sizes were determined to be typically $\sim$ 0.07 pc. Both these models and those of Evans et al. (2001) ignore the effects of magnetic fields.

Magnetic fields have been suggested as a means of providing support against gravitational collapse of the core. The effects of ambipolar diffusion on the early stages of core formation and collapse have been studied theoretically by Mouschovias and collaborators. These models produce the same general results – the central regions of an initially magnetically subcritical cloud evolve under the influence of ambipolar diffusion to form a magnetically supercritical core which then collapses dynamically. The surrounding envelope is unaffected by the ambipolar diffusion occurring in the center of the cloud and remains magnetically supported. The supercritical core consists of a nearly uniform density central region embedded in a region where the density varies as a power law $n(r) \propto r^{-s}$ where s is between 1.5 and 1.7 (Ciolek & Mouschovias 1994, 1995; Basu & Mouschovias 1994, 1995a,b).

One problem with these ambipolar diffusion models is that they predict cores which are oblate whereas observations find that the majority of cores are prolate (Myers et al. 1991). Additionally, Ward–Thompson et al. (1999) find that the timescales for protostellar collapse deduced from statistical analysis of pre–protostellar core observations are not consistent with the ambipolar diffusion model timescales.

Lizano & Shu (1989) modeled the formation of a dense core out of a more diffuse back-

coming paper which will combine the ISO data, the molecular line data and submillimeter data.

Having said that it is still our view that CO (and other molecules) are depleted in the center of the L1498 core. The CO emission peaks are not coincident with the dust emission peak and instead are to each side of it, where peaks in CS and CCS are also seen (Kuiper et al. 1996). Only NH_3 peaks in the center of the core where ΔI_{200} emission maxima is seen. This distribution is consistent with chemical models of collapsing regions which predict that NH_3 will remain in the gas longer than CO (Rawlings et al. 1992).

4. Conclusions

We have studied the FIR emission from three pre–protostellar cores: B133, L1498 and B68. We have determined the radial density profiles for each core and found that they could be fitted by a series of power laws. In the center of the core the distribution is relatively flat with $n \propto r^{-1.2}$. At $r > 10^{17}$ cm the distribution approaches r^{-2}. At the edges of B133 and B68 the density profiles are very steep with $r^{-\alpha}$ where $\alpha = 4 - 6$ ($r > 5 \times 10^{17}$ cm).

Our results are in general agreement with previous observational studies, which have also found a flattened density distribution towards the center of pre–protostellar cores. In common with most other workers we have characterized this by a series of power laws, in contrast to Shirley et al. (2000) who did not find power laws to give an accurate description of their data. Our results are also consistent with many of the theoretical models of core formation. They do not fit the singular isothermal sphere which is often used as the starting point for protostellar collapse but this may be because the cores are not sufficiently evolved to have reached this state or because of magnetic or other support in the core center.

Our results demonstrate the importance of an accurate determination of the dust temperature. Even a 1 K difference in T_d can result in a factor of 2.7 in the calculated column densities, masses and number densities. The choice of dust emissivity also has a crucial effect on these results, with the values of σ ($=\tau/N_H$) available in the literature differing by up to a factor of 4.

The relative stability of the cores varies with radius. The inner regions in all three cores appear to be less bound than the outer layers, with the result that the outer layers seem to be confining the inner ones.

Observations at many different wavelengths are required in order to fully characterize the physical structure of pre–protostellar cores. Longer wavelength observations are less

temperature dependent than the FIR measurements discussed here and can be used as a means of calibrating the column density estimates. Shorter wavelength observations will probe the envelope and will provide information about the dust in this region, which will enable estimates of molecular depletion to be made.

This research was conducted at the Jet Propulsion Laboratory, California Institute of Technology under partial support from the National Aeronautics and Space Administrations ADP program. We are grateful to Nanyao Lu and Mary Barsony for valuable assistance in the reduction and analysis of the ISOPHOT data.

The ISOPHOT data presented in this paper was reduced using PIA, which is a joint development by the ESA Astrophysics Division and the ISOPHOT consortium, with the collaboration of the Infrared Analysis and Processing Center (IPAC) and the Instituto de Astrofisica de Canarias (IAC).

Fig. 1.— ISOPHOT observations of B133 at 200 μm. Coordinates are given in J2000. (a) 100 μm with contours at intervals of 1 MJy/sr between 37 and 46 MJy/sr. (b) 200 μm with contours at intervals of 10 MJy/sr from 70 to 150 MJy/sr (c) I_{200} vs I_{100} scatter plot showing two component fit. (d) ΔI_{200} with contours at intervals of 4 MJy/sr between 4 and 48 MJy/sr.

Fig. 2.— ISOPHOT observations of B133 at 160 μm. (a) 160 μm with contours at intervals of 5 MJy/sr between 70 and 110 MJy/sr (b) I_{160} vs I_{100} scatter plot showing two components (c) I_{200} vs I_{160} scatter plot showing only one grain component suggesting that the emission at these two wavelengths arises from the same grain population

Fig. 3.— ISOPHOT observations of L1498. Coordinates are given in J2000. (a) 100 μm with contours at 0.5 MJy/sr intervals between 16 and 20.5 MJy/sr (b) 200 μm with contours at 5 MJy/sr intervals between 45 and 75 MJy/sr (c) I_{200} vs I_{100} showing the flattening of the 100 μm emission at high values of I_{200} indicating a two populations of dust grains. The fits to the data are shown (d) The cold central core as traced in the 200 μm emission, Δ I_{200}, determined by the subtraction process detailed in this paper. Contours are at 1 MJy/sr intervals between 1 and 8 MJy/sr. The peak Δ I_{200} flux is 8.75 MJy/sr.

Fig. 4.— ISOPHOT observations of B68. Coordinates are given in J2000. (a) 100 μm with contours at intervals of 1 MJy/sr between 42 and 50 MJy/sr. (b) 200 μm with contours at intervals of 5 MJy/sr from 100 to 135 MJy/sr (c) I_{200} vs I_{100} scatter plot showing two component fit. (d) Δ I_{200} with contours at intervals of 2 MJy/sr between 2 and 24 MJy/sr

Fig. 5.— Column densities for B133 calculated at the position of the 1300 μm observation for a range of temperatures using $\Delta I(200)$, $\Delta I(160)$ and 1300 μm data.

Fig. 6.— The radial mass distribution for (a) B133, (b) L1498 and (c) B68. Also shown are the 3rd order polynomial fits to the data

Fig. 7.— The radial density distributions for (a) B133, (b) L1498 and (c) B68

REFERENCES

Abergel, A., Bernard, J. P., Boulanger, F., Cesarsky, C., Desert, F. X., Falgarone, E., Lagache, F., Perault, M., Puget, J.–L., Reach, W. T., Nordh, L., Olofsson, G., Huldtgren, M., Kaas, A. A., André, P., Bontemps, S., Burgdorf, M., Copet, E., Davies, J., Montmerle, T., Persi, P., Sibille, F. 1996 A&A, 315, 329

Abergel, A., Bernard, J. P., Boulanger, F., Desert, F.-X., Lagache, G., Puget, J. L., Reach, W. T., Falgarone, E., Nordh, L., Olofsson, G., André, P., Bacmann, A., Ristorcelli, I. 1998, in ASP Conf Ser. 132, Star formation with the Infrared Space Observatory, ed J. Yun, R. Liseau, (San Francisco: ASP), 220

André, P., Ward–Thompson, D., Motte, F. 1996, A&A, 314, 625

Avery, L. W., White, G. J., Williams, I. P., Cronin, N. 1987, ApJ, 312, 848

Bacmann, A., André, P., Puget, J.–L., Abergel, A., Bontemps, S., Ward–Thompson, D. 2000, A&A, 361, 555

Basu, S., Mouschovias, T. Ch. 1995a, ApJ, 452, 386

Basu, S., Mouschovias, T. Ch. 1995b, ApJ, 453, 271

Basu, S., Mouschovias, T. Ch. 1994, ApJ, 432, 720

Benson, P. J., Myers, P. C. 1989, ApJS, 71, 89

Benson, P. J., Caselli, P., Myers, P. C. 1998, ApJ, 506, 743

Chièze, J.–P., Pineau des Forêts, G. 1987, A&A, 183, 98

Ciolek, G. E., Mouschovias, T. Ch. 1995, ApJ, 454, 194

Ciolek, G. E., Mouschovias, T. Ch. 1994, ApJ, 427, 839

Cox, P., Mezger, P. G. 1989, Astron. Astrophys. Rev, 1, 49 (CM89)

Draine, B. T., Lee, H. M. 1984, ApJ, 285, 89

Ehrenfreund, P., Schutte, W. A. 2000, in IAU Symp. No. 197, Astrochemistry: From Molecular Clouds to Planetary Systems, ed Y. C. Minh & E. F. van Dishoeck (San Francisco: ASP), 135

Evans, N. J., II, Rawlings, J. M. C., Shirley, Y. L., Mundy, L. G. 2001, ApJ, submitted

Falgarone, E., Puget, J. L. 1985, A&A, 142, 157

Fiebig, D. 1990, Ph.D. Thesis, Friedrich–Wilhelms Univ, Bonn

Foster, P. N., Chevalier, R. A. 1993, ApJ, 416, 303

Frerking, M. A., Langer, W. D., Wilson, R. W. 1982, ApJ, 262, 590

Fuller, G. A., Myers, P. C. 1993, ApJ, 418, 273

Gabriel, C., Acosta–Pulido, J., Heinrichsen, I., Morris, H., Skaley, D., Tai, W. M. 1997, in ASP Conf. Ser. 125, Astronomical Data Analysis Software and Systems VI, ed G. Hunt & H. Payne (San Francisco: ASP), 108

Henriksen, R., André, P., Bontemps, S. 1997, A&A, 323, 549

Hildebrand, R. H. 1983, QJRAS, 24, 267

Jijina, J., Myers, P. C., Adams, F. C. 1999, ApJS, 125, 161

Kuiper, T. B. H., Langer, W. D., Velusamy, T. 1996, ApJ, 468, 761

Laureijs, R. J., Haikala, L., Burgdorf, M., Clark, F. O., Liljestroem, T., Mattila, K., Prusti, T. 1996, A&A, 315, 317

Lefloch, B., Castets, A., Cernicharo, J., Langer, W. D., Zylka, R. 1998, A&A, 334, 269

Lemme, C., Wilson, T. L., Tieftrunk, A. R., Henkel. C. 1996, A&A, 312, 585

Lemme, C., Walmsley, C. M., Wilson, T. L., Muders, D. 1995, A&A, 302, 509

Lizano, S., Shu, F. H. 1989, ApJ, 342, 834

MacLaren, I., Richardson, K. M., Wolfendale, A. W. 1988, ApJ, 333, 821

Mauersberger, R., Wilson, T. L., Mezger, P. G., Gaume, R., Johnston, K. J. 1992, A&A, 256, 640

Mezger, P. G., Sievers, A. W., Haslam, C. G. T., Kreysa, E., Lemke, R., Mauersberger, R., Wilson, T. L. 1992, A&A, 256, 631

Myers, P. C., Fuller, G., Goodman, A. A., Benson, P. J. 1991, ApJ, 376, 561

Myers, P. C., Linke, R. A., Benson, P. J. 1983, ApJ, 264, 517

Rawlings, J. M. C., Hartquist, T. W., Menten, K. M., Williams, D. A. 1992, MNRAS, 255, 471

Shirley, Y. L., Evans, N. J., II, Rawlings, J. M. C. & Gregersen, E. M. 2000, ApJS, 131, 249

Shu, F. H. 1977, ApJ, 214, 488

Ward–Thompson, D., Motte, F., André, P. 1999, MNRAS, 305, 143

Ward–Thompson, D., Scott, P. F., Hills, R. E., André, P. 1994, MNRAS, 268, 276

Willacy, K., Langer, W. D., Velusamy, T. 1998, ApJ, 507, L171 (Paper I)

Wolkovitch, D., Langer, W. D., Goldsmith, P. F., Heyer, M. 1997, ApJ, 477, 241

Fig 6b

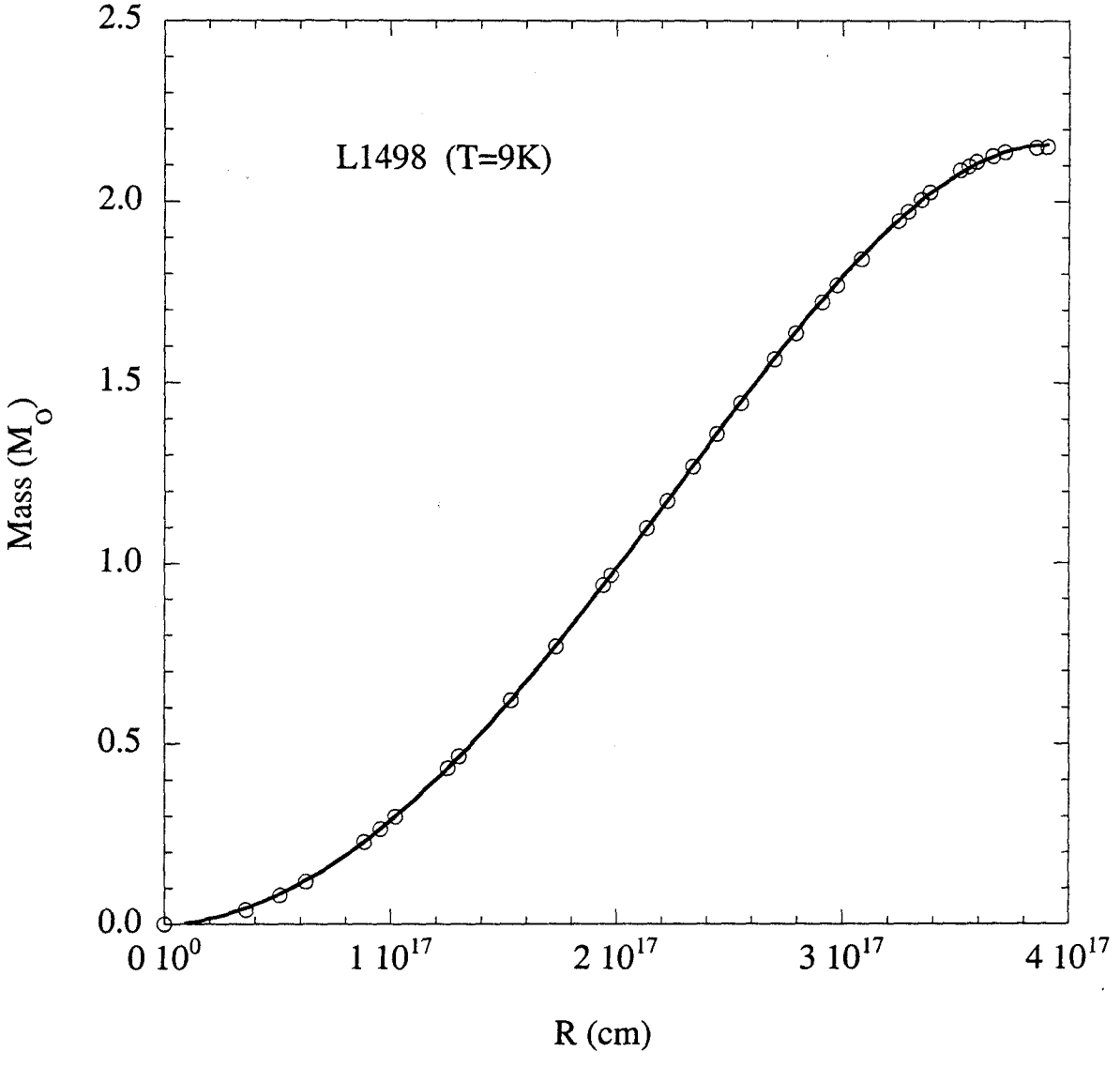
L1498 (T=9K)
Mass (M_o)
2.5
2.0
1.5
1.0
0.5
0.0
0 10^0
1 10^{17}
2 10^{17}
3 10^{17}
4 10^{17}
R (cm)

Table 1. Physical parameters of sources studied. For B133 and L1498 the 1300 μm data is taken from Ward–Thompson et al. (1994) and (1999) respectively. The positions given are the center of the ISO maps and the position of the 1300 μm observations. 1300 μm data is not available for B68.

Source	ISO position		Distance	1300 μm position		1300 μm flux
	RA (2000)	Dec (2000)	(pc)	RA (2000)	Dec (2000)	(mJy per 13 arcsec)
L1498	04 10 52.10	25 09 58.9	140	04 10 51.4	25 10 16	10
B133	19 06 8.65	-06 51 57.2	200[a]	19 06 08.8	-06 52 20	45
B68	17 22 37.72	-23 50 2.3	200[b]	...	...	

[a]The distance to B133 is uncertain. This estimate is taken from Ward–Thompson et al. (1994).

[b]From Jijina et al. (1999).

Table 2. (a) Core masses for B133 determined from ΔI_{200} for $T_d = 8$ and 9 K. Also shown are the core virial masses calculated using the method of MacLaren et al. (1988).

Radius (cm)	Mass derived from ΔI_{200}		Calculated virial mass	
	T = 8 K	T = 9 K	$\rho \propto 1/r$	$\rho \propto 1/r^{-2}$
6.0 (17)	42.9	15.8	15.1	10.0
5.5 (17)	40.4	14.9	13.8	9.2
5.0 (17)	37.9	13.7	12.6	8.3
4.5 (17)	33.4	12.3	11.3	7.5
4.0 (17)	29.1	10.7	10.1	6.7
3.5 (17)	24.5	9.0	8.8	5.8
3.0 (17)	19.7	7.3	7.5	5.0
2.5 (17)	15.0	5.5	6.3	4.2
2.0 (17)	10.5	3.8	5.0	3.3
1.5 (17)	6.4	2.4	3.8	2.5
1.0 (17)	3.1	1.1	2.5	1.7
0.8 (17)	2.0	0.8	2.0	1.3
0.4 (17)	...	...	1.0	0.7

Table 2. (b) As for Table 2(a) but for L1498

Radius (cm)	Mass derived from ΔI_{200}		Calculated virial mass	
	T = 8 K	T = 9 K	$\rho \propto 1/r$	$\rho \propto 1/r^{-2}$
6.0 (17)	...	...	10.7	7.1
5.5 (17)	...	...	9.8	6.5
5.0 (17)	...	...	8.9	5.5
4.5 (17)	...	...	8.0	4.9
4.0 (17)	5.9	2.2	7.1	4.4
3.5 (17)	5.6	2.1	6.3	3.8
3.0 (17)	4.9	1.8	5.3	3.3
2.5 (17)	3.8	1.4	4.5	2.7
2.0 (17)	2.7	1.0	3.4	2.2
1.5 (17)	1.6	0.6	2.7	1.6
1.0 (17)	0.8	0.3	1.8	1.1
0.8 (17)	0.6	0.2	1.3	0.9
0.4 (17)	0.2	0.1	0.7	0.4

Table 2. (c) As for Table 2(a) but for B68

Radius (cm)	Mass derived from ΔI_{200}		Calculated virial mass	
	T = 8 K	T = 9 K	$\rho \propto 1/r$	$\rho \propto 1/r^{-2}$
6.0 (17)	38.1	14.0	10.7	7.1
5.5 (17)	36.5	13.4	9.8	6.5
5.0 (17)	33.9	12.5	8.9	5.5
4.5 (17)	30.5	11.2	8.0	4.9
4.0 (17)	26.4	9.7	7.1	4.4
3.5 (17)	22.1	8.1	6.3	3.8
3.0 (17)	17.5	6.5	5.3	3.3
2.5 (17)	13.1	4.8	4.5	2.7
2.0 (17)	8.9	3.3	3.4	2.2
1.5 (17)	5.3	2.0	2.7	1.6
1.0 (17)	2.5	0.9	1.8	1.1
0.8 (17)	1.6	0.6	1.3	0.9
0.4 (17)	...	...	0.7	0.4

Table 3. The radial H_2 density distributions determined in the cores from Equation 6 assuming $T_d = 9$ K.

Radius (cm)	$n(H_2)$		
	L1498	B133	B68
6.0 (17)	···	1.6 (3)	8.0 (2)
5.5 (17)	···	2.6 (3)	1.9 (3)
5.0 (17)	···	3.8 (3)	3.3 (3)
4.5 (17)	···	5.5 (3)	5.0 (3)
4.0 (17)	···	7.5 (3)	7.0 (3)
3.5 (17)	1.2 (3)	1.1 (4)	1.0 (4)
3.0 (17)	2.9 (3)	1.5 (4)	1.4 (4)
2.5 (17)	5.0 (3)	2.0 (4)	1.9 (4)
2.0 (17)	7.5 (3)	2.9 (4)	2.7 (4)
1.5 (17)	1.2 (4)	4.5 (4)	3.9 (4)
1.0 (17)	1.9 (4)	7.5 (4)	6.5 (4)
8.0 (16)	2.5 (4)	1.1 (5)	8.5 (4)
4.0 (16)	5.5 (4)	···	···

Table 4. Power law fits to density distribution in each core where $n(r) \propto r^{-\alpha}$. Inner refers to $r < 2 \times 10^{17}$ cm for B133 and B68 and $r < 10^{17}$ cm for L1498, middle: $1\text{–}2 \times 10^{17} < r < 5 \times 10^{17}$ cm; outer: $r > 5 \times 10^{17}$ cm

Source	α		
	Inner	Middle	Outer
B133	1.32	1.89	4.27
L1498	1.16	1.69	···
B68	1.22	2.02	6.34

Table 5. Observed line widths for some molecules in our cores. The non–thermal line widths are determined from equation 7 assuming a gas temperature of 10 K.

Source	NH_3	C_3H_2	HC_7N	Δv_{nt}	$\Delta v(H_2)$
L1498[a]	0.24	0.26	0.14	0.17	0.51
B133[b]	0.44	0.46	···	0.41	0.63
B68[c]	0.28	···	···	0.23	0.53

[a]Molecular data is taken from Kuiper et al. (1996).

[b]Molecular data is taken from Jijina et al. (1999) and Benson et al. 1998.

[c]Estimate of NH_3 line width is from Jijina et al. (1999).

fig 1.

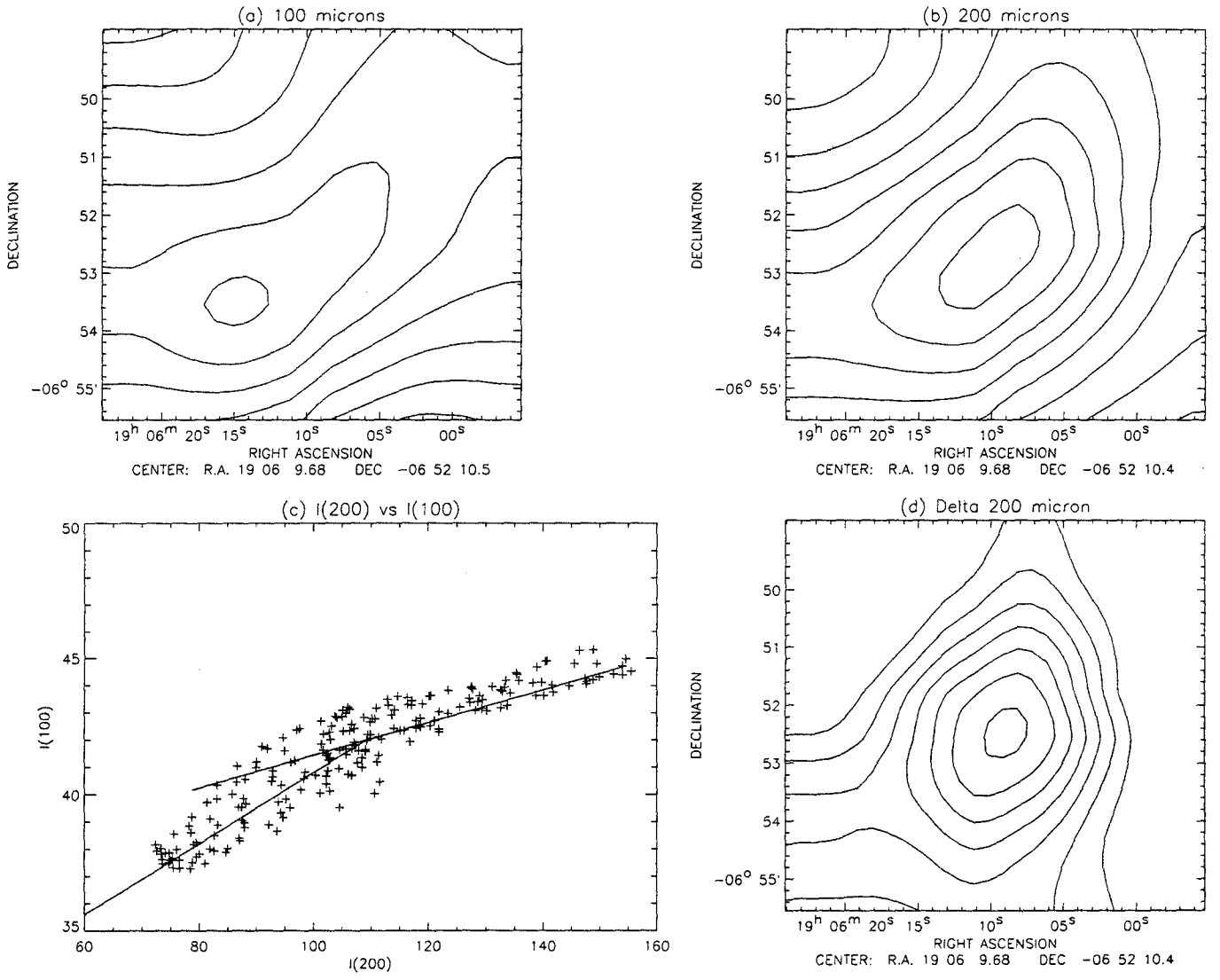
(a) 100 microns
DECLINATION
50
51
52
53
54
-06° 55'
19h 06m 20s 15s 10s 05s 00s
RIGHT ASCENSION
CENTER: R.A. 19 06 9.68 DEC -06 52 10.5
(b) 200 microns
DECLINATION
50
51
52
53
54
-06° 55'
19h 06m 20s 15s 10s 05s 00s
RIGHT ASCENSION
CENTER: R.A. 19 06 9.68 DEC -06 52 10.4
(c) I(200) vs I(100)
I(100)
50
45
40
35
60
80
100
120
140
160
I(200)
(d) Delta 200 micron
DECLINATION
50
51
52
53
54
-06° 55'
19h 06m 20s 15s 10s 05s 00s
RIGHT ASCENSION
CENTER: R.A. 19 06 9.68 DEC -06 52 10.4

Fig2

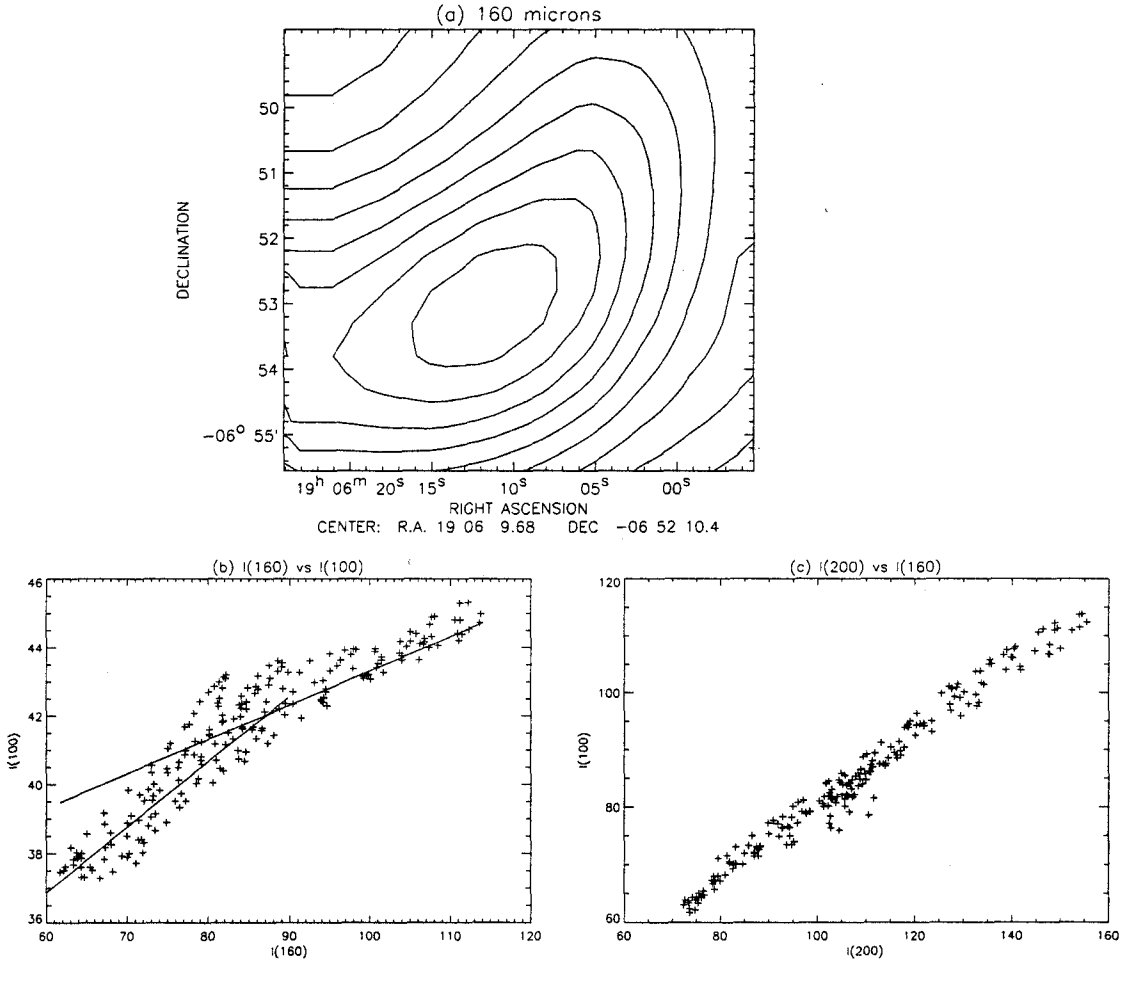
(a) 160 microns
DECLINATION
50
51
52
53
54
−06° 55'
19h 06m 20s 15s 10s 05s 00s
RIGHT ASCENSION
CENTER: R.A. 19 06 9.68 DEC −06 52 10.4
(b) I(160) vs I(100)
I(100)
I(160)
(c) I(200) vs I(160)
I(100)
I(200)

Fg 3

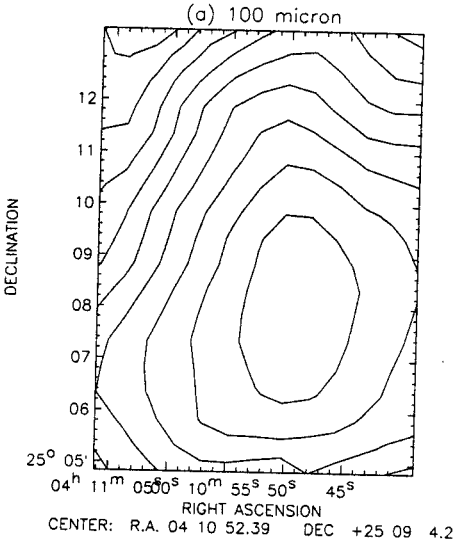
(a) 100 micron
DECLINATION
12
11
10
09
08
07
06
25° 05'
04h 11m 05s 00s 10m 55s 50s 45s
RIGHT ASCENSION
CENTER: R.A. 04 10 52.39 DEC +25 09 4.2

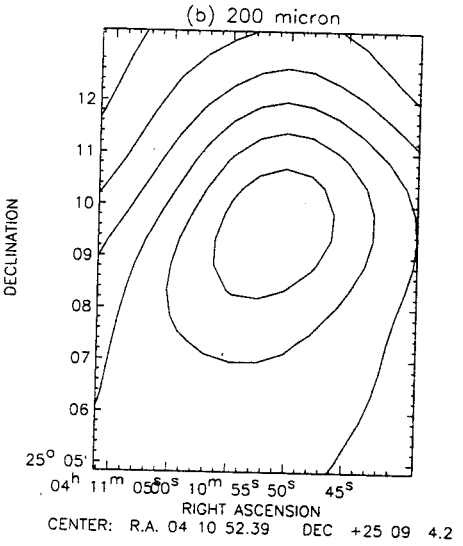
(b) 200 micron
DECLINATION
12
11
10
09
08
07
06
25° 05'
04h 11m 05s 00s 10m 55s 50s 45s
RIGHT ASCENSION
CENTER: R.A. 04 10 52.39 DEC +25 09 4.2

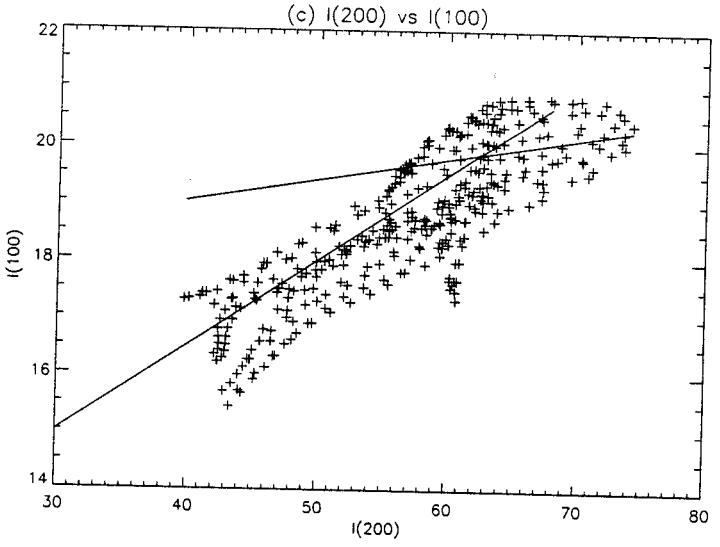
(c) I(200) vs I(100)
I(100)
22
20
18
16
14
30
40
50
60
70
80
I(200)

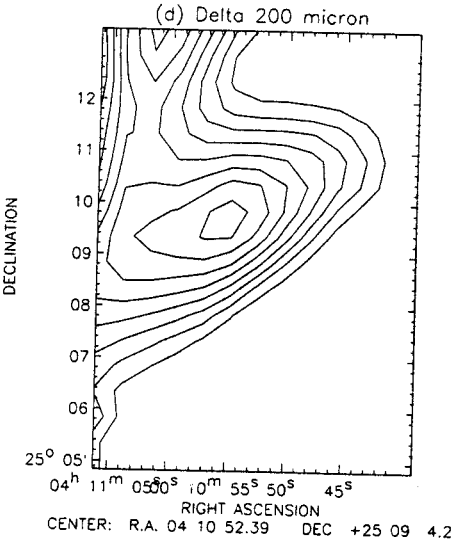
(d) Delta 200 micron
DECLINATION
12
11
10
09
08
07
06
25° 05'
04h 11m 05s 00s 10m 55s 50s 45s
RIGHT ASCENSION
CENTER: R.A. 04 10 52.39 DEC +25 09 4.2

Fig 4

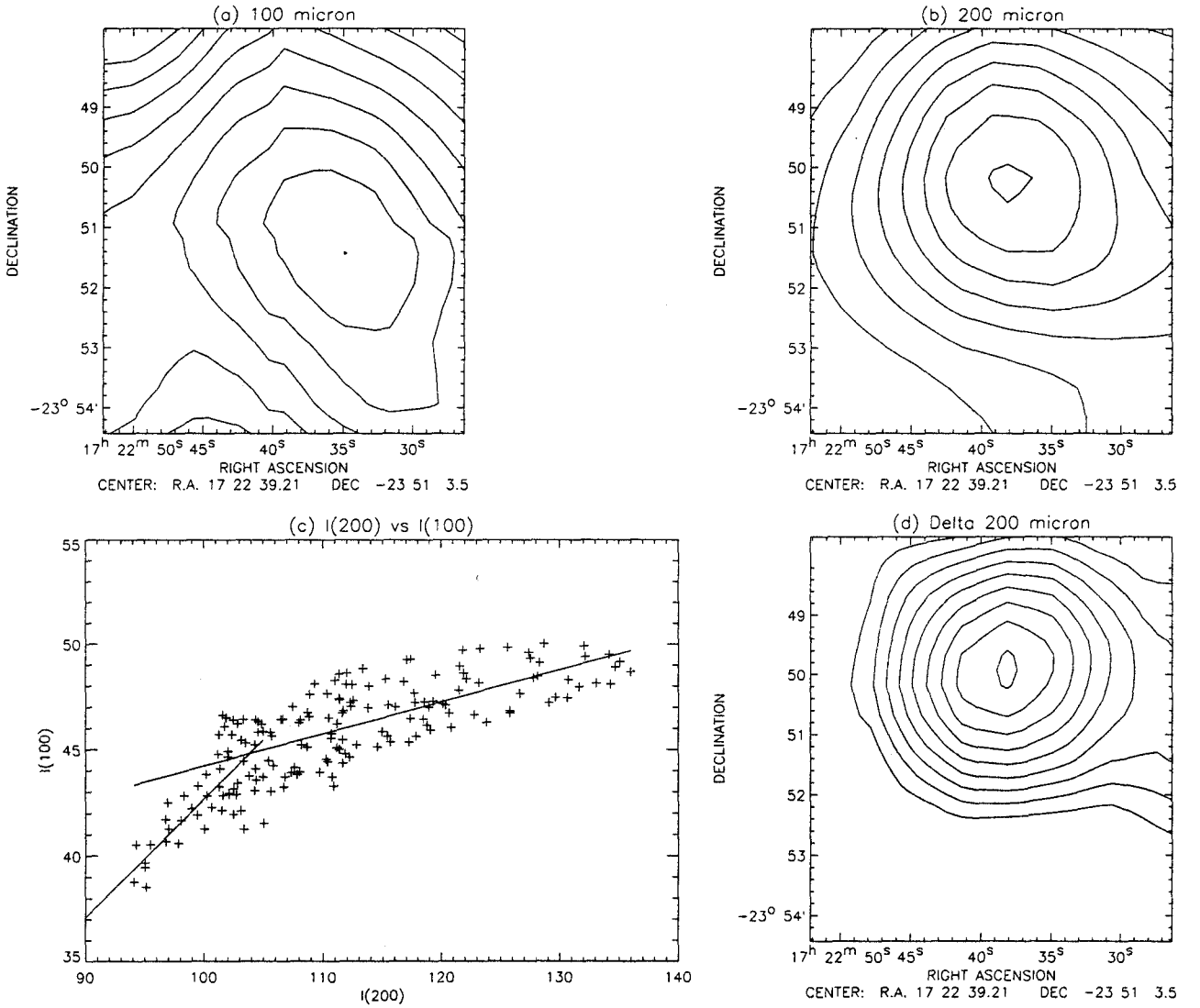
(a) 100 micron
DECLINATION
49
50
51
52
53
-23° 54'
17h 22m 50s 45s 40s 35s 30s
RIGHT ASCENSION
CENTER: R.A. 17 22 39.21 DEC -23 51 3.5
(b) 200 micron
DECLINATION
49
50
51
52
53
-23° 54'
17h 22m 50s 45s 40s 35s 30s
RIGHT ASCENSION
CENTER: R.A. 17 22 39.21 DEC -23 51 3.5
(c) I(200) vs I(100)
I(100)
55
50
45
40
35
90 100 110 120 130 140
I(200)
(d) Delta 200 micron
DECLINATION
49
50
51
52
53
-23° 54'
17h 22m 50s 45s 40s 35s 30s
RIGHT ASCENSION
CENTER: R.A. 17 22 39.21 DEC -23 51 3.5

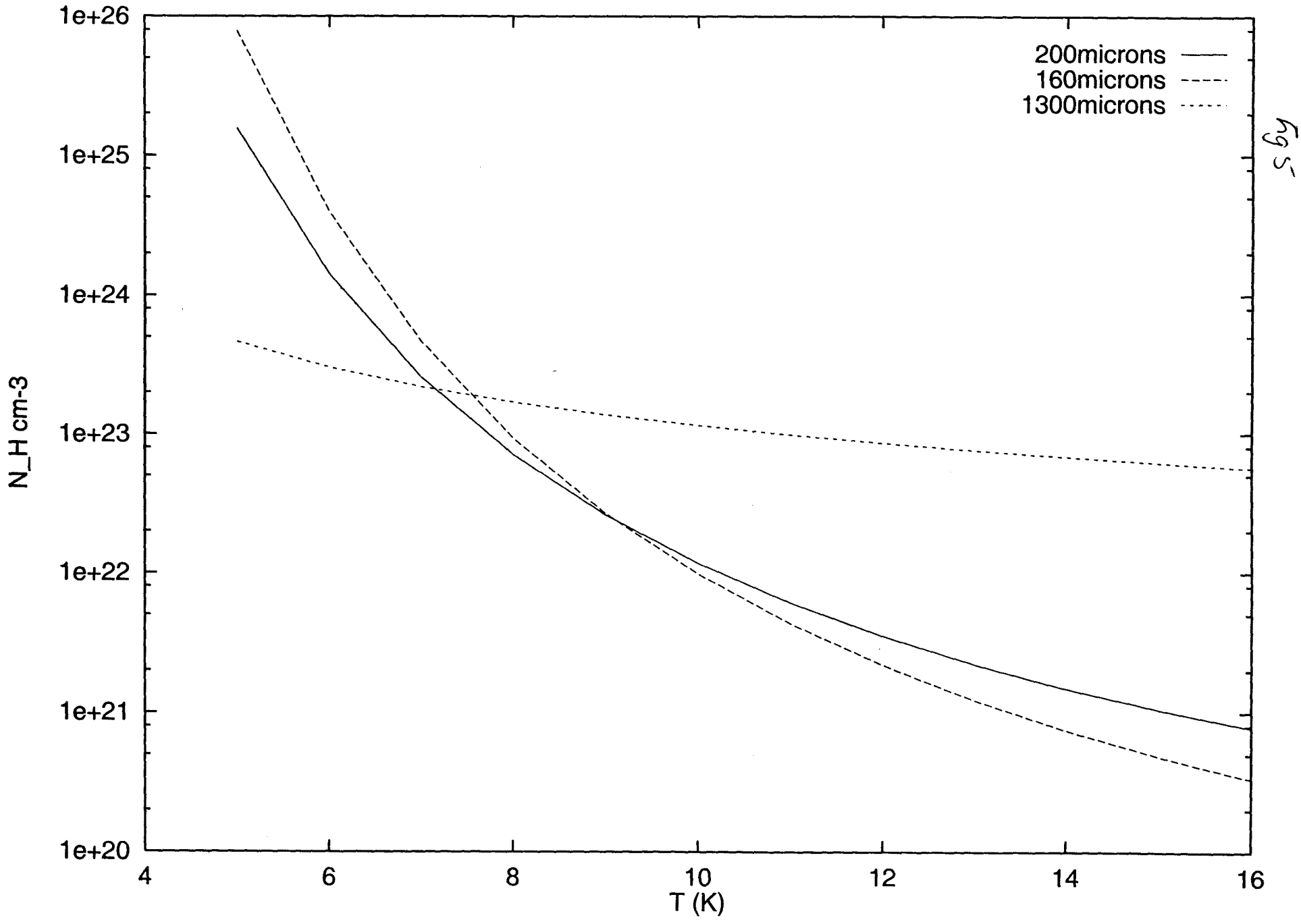
1e+26
1e+25
1e+24
1e+23
1e+22
1e+21
1e+20
N_H cm-3
4
6
8
10
12
14
16
T (K)
200microns
160microns
1300microns

fig 5

Fig 6a

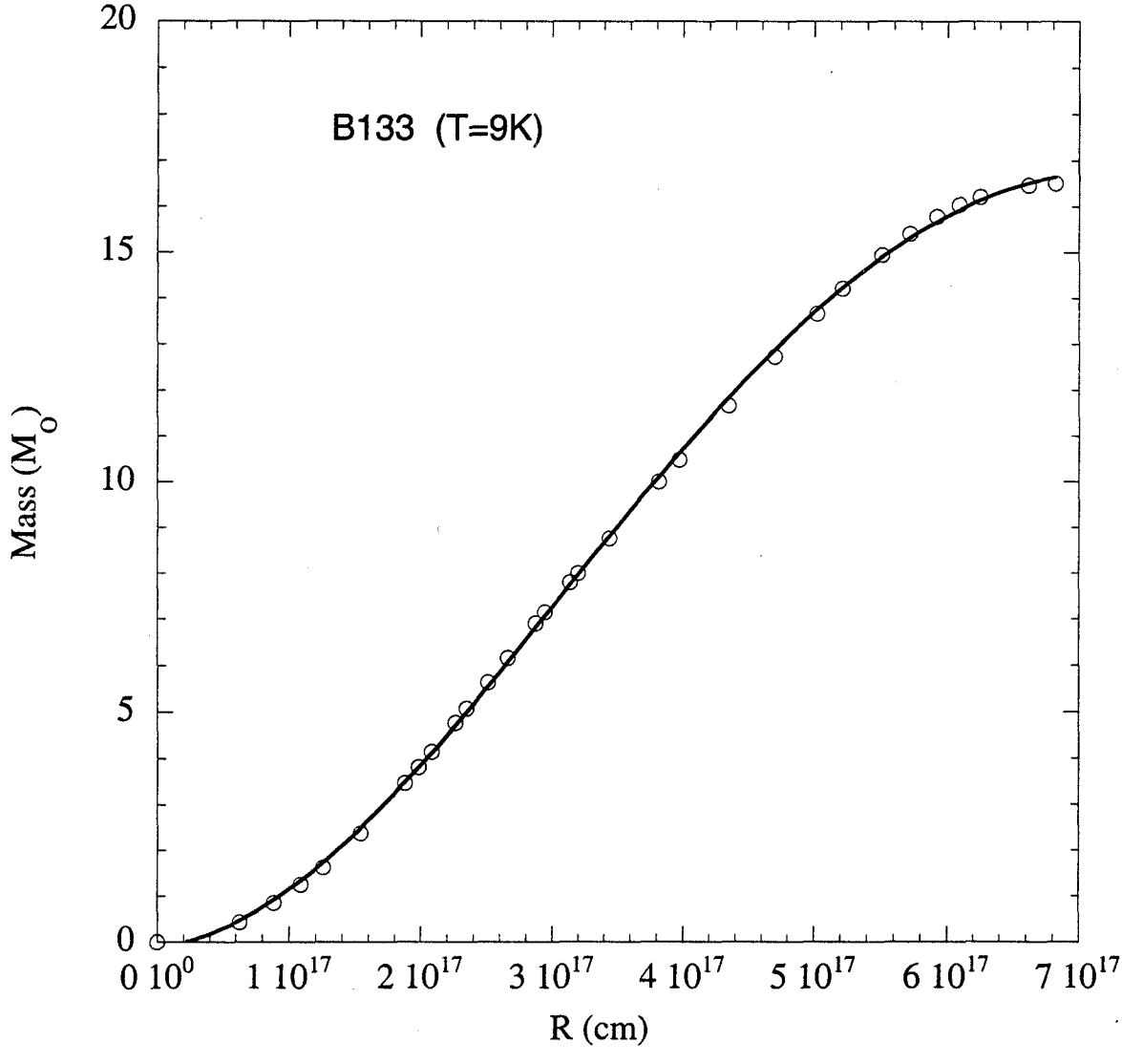
B133 (T=9K)
Mass (M_o)
R (cm)
0
5
10
15
20
0 10^0
1 10^{17}
2 10^{17}
3 10^{17}
4 10^{17}
5 10^{17}
6 10^{17}
7 10^{17}

Fig 6c

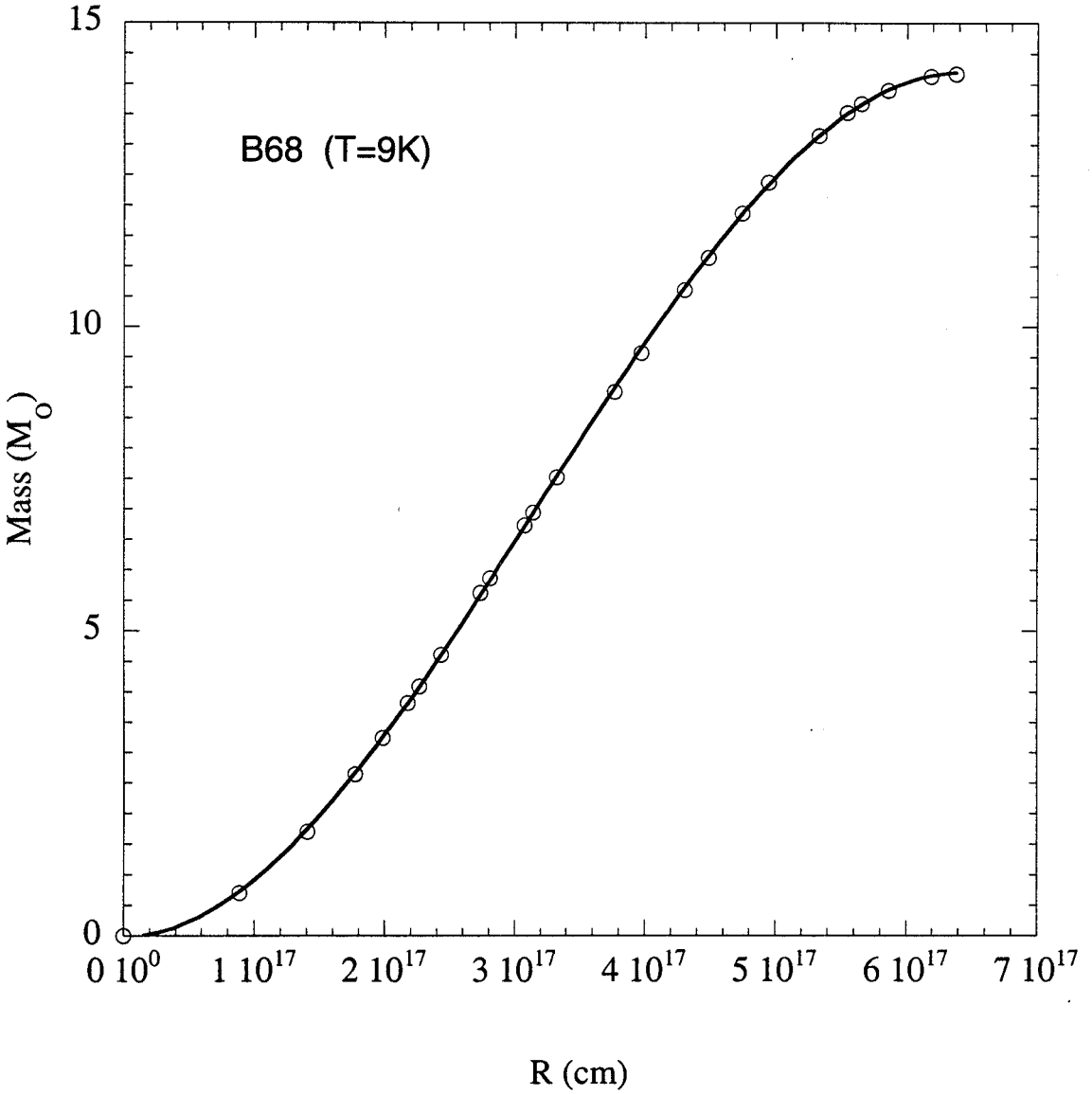
B68 (T=9K)
Mass (M_o)
R (cm)
0
5
10
15
0 10^0
1 10^{17}
2 10^{17}
3 10^{17}
4 10^{17}
5 10^{17}
6 10^{17}
7 10^{17}

Fig 7a

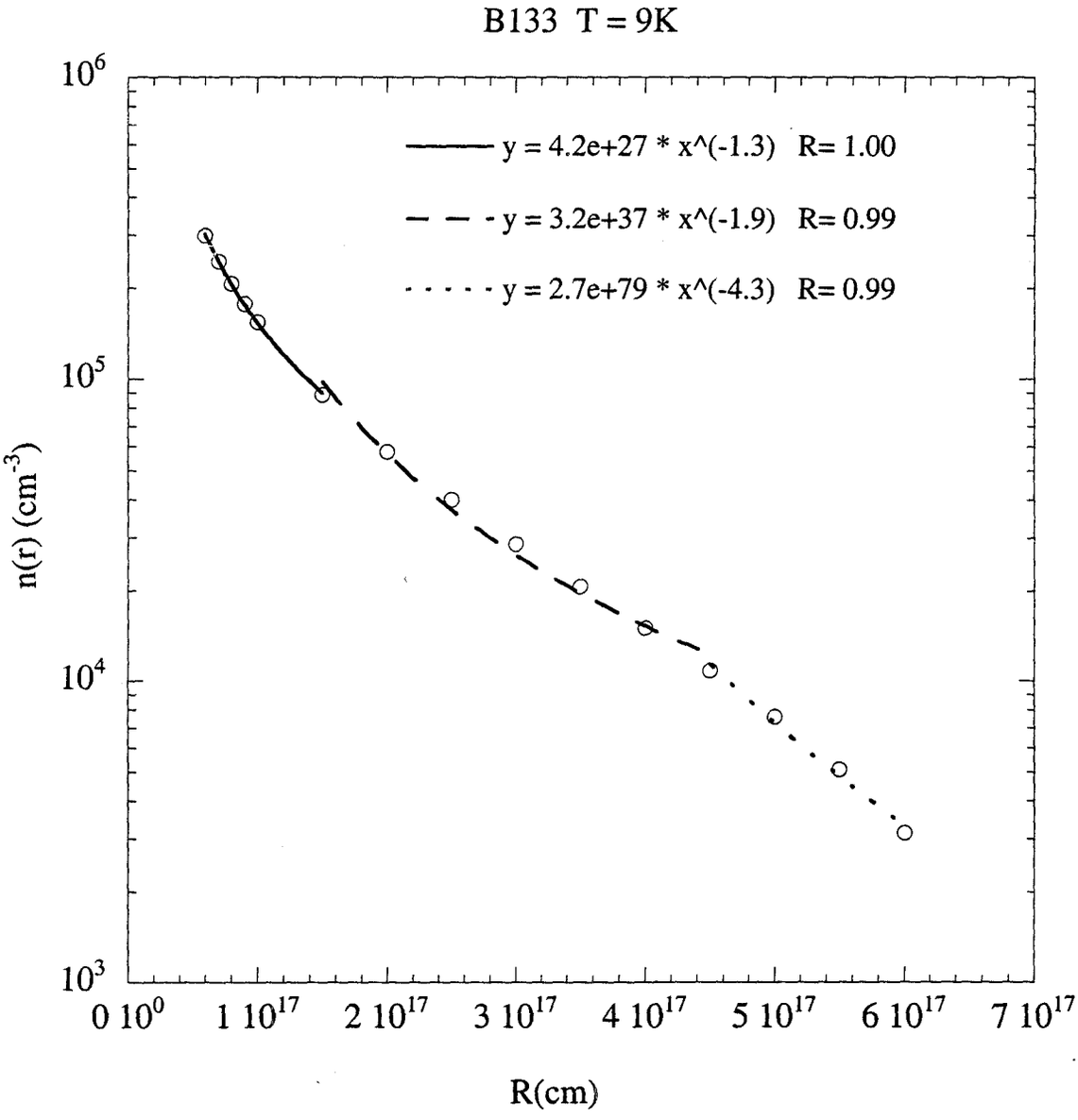
B133 T = 9K
y = 4.2e+27 * x^(-1.3) R= 1.00
y = 3.2e+37 * x^(-1.9) R= 0.99
y = 2.7e+79 * x^(-4.3) R= 0.99
n(r) (cm-3)
10^6
10^5
10^4
10^3
0 10^0
1 10^17
2 10^17
3 10^17
4 10^17
5 10^17
6 10^17
7 10^17
R(cm)

Fig 7b

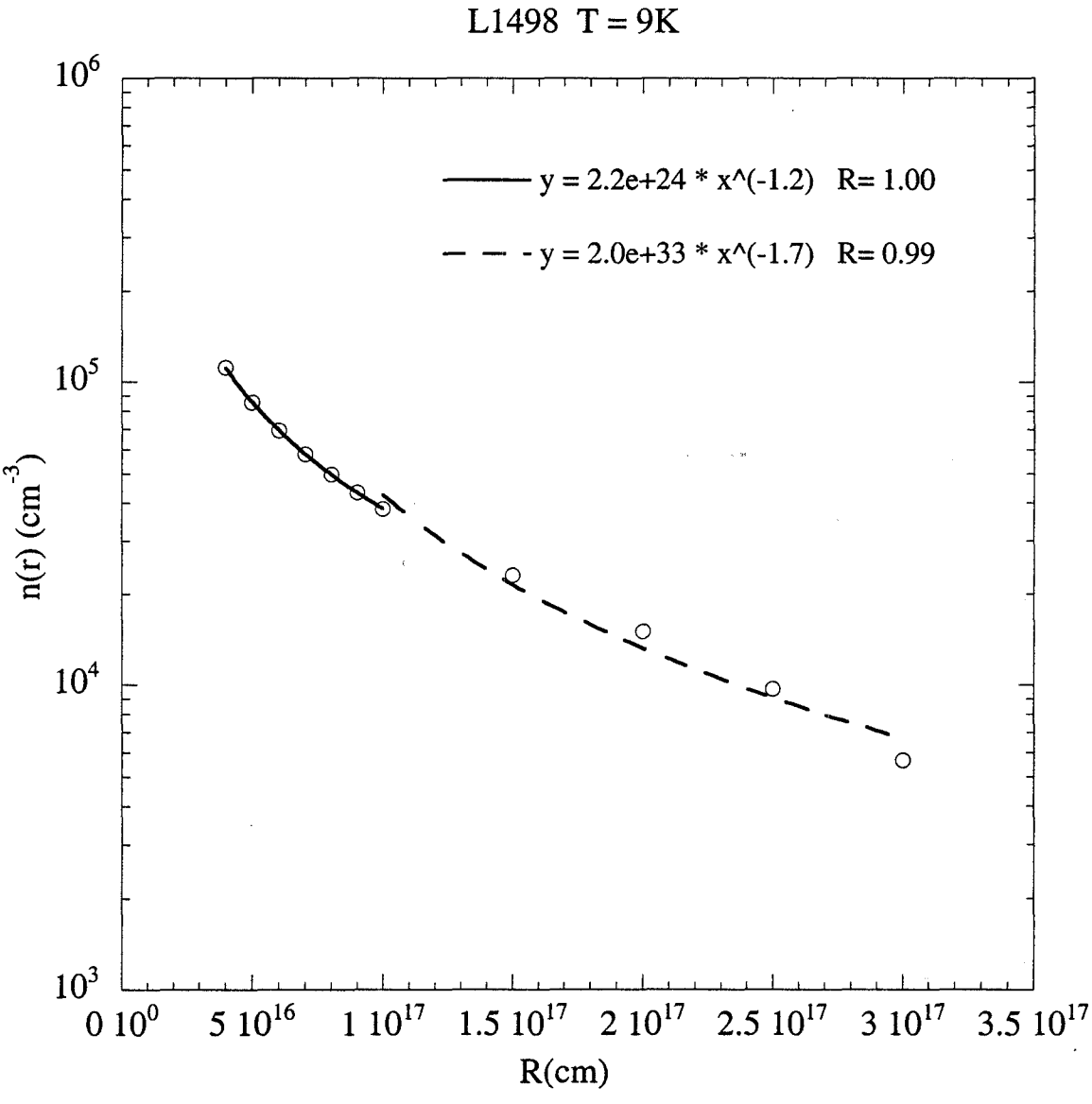
L1498 T = 9K
y = 2.2e+24 * x^(-1.2) R= 1.00
y = 2.0e+33 * x^(-1.7) R= 0.99
n(r) (cm^-3)
10^6
10^5
10^4
10^3
0 10^0
5 10^16
1 10^17
1.5 10^17
2 10^17
2.5 10^17
3 10^17
3.5 10^17
R(cm)

Fig 7c.

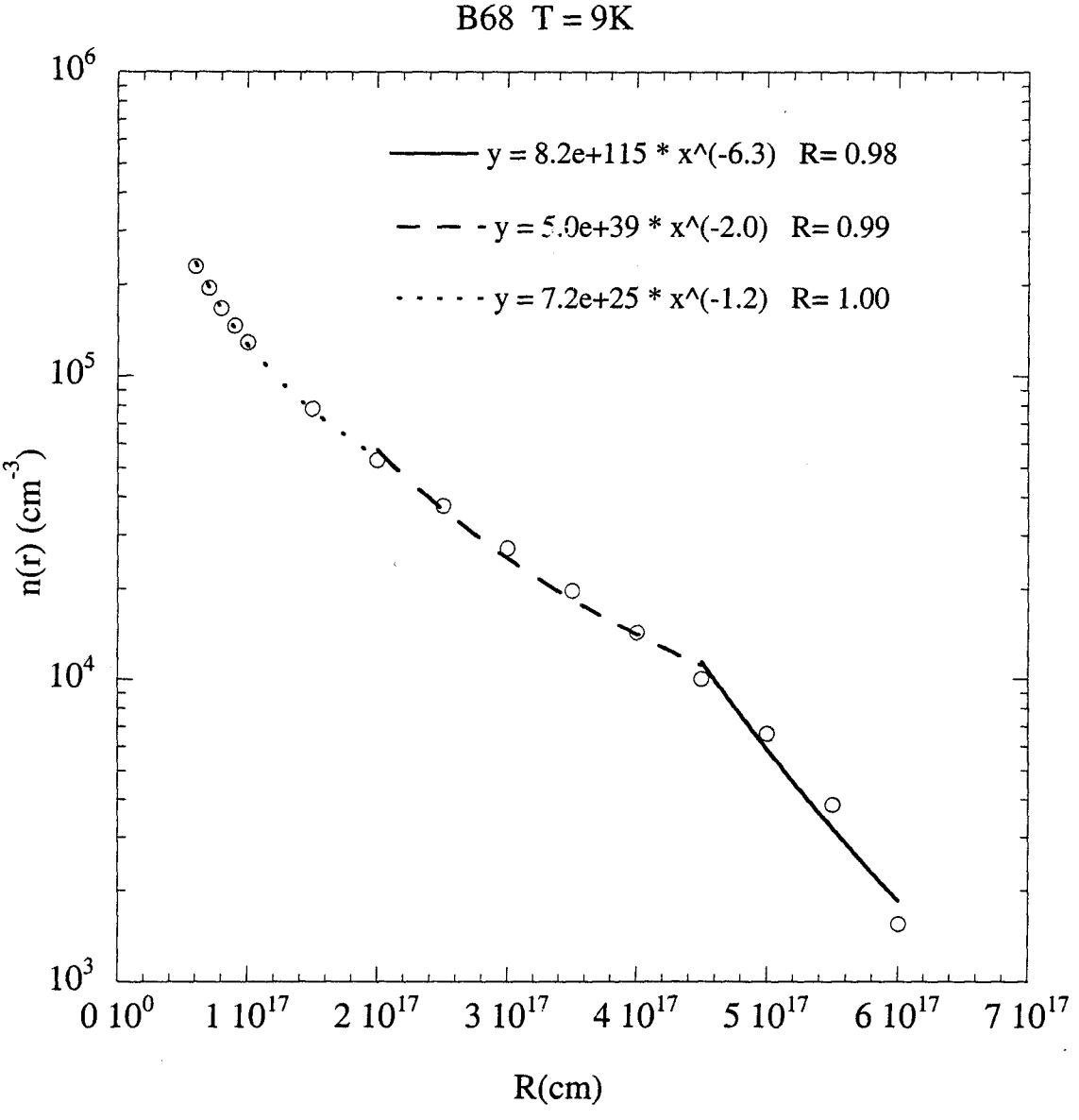
B68 T = 9K
y = 8.2e+115 * x^(-6.3) R= 0.98
y = 5.0e+39 * x^(-2.0) R= 0.99
y = 7.2e+25 * x^(-1.2) R= 1.00
n(r) (cm-3)
10^6
10^5
10^4
10^3
0 10^0
1 10^17
2 10^17
3 10^17
4 10^17
5 10^17
6 10^17
7 10^17
R(cm)